High-Density 3D-Boron Nitride and 3D-Graphene for High-Performance Nano–Thermal Interface Material

Loeblein, Manuela; Tsang, Siu Hon; Pawlik, Matthieu; Phua, Eric Jian Rong; Yong, Han; Zhang, Xiao Wu; Gan, Chee Lip; Teo, Edwin Hang Tong

2017

High Density 3D-Boron Nitride & 3D-Graphene for High Performance Nano-Thermal Interface Material

Manuela Loeblein,[†,‡,$] Siu Hon Tsang,[||] Matthieu Pawlik,[‡] Eric Jian Rong Phua,[||, #] Han Yong,[$] Xiao Wu Zhang,[$] Chee Lip Gan[||,#] and Edwin Hang Tong Teo[†,#,]*

[†]School of Electrical and Electronic Engineering, Nanyang Technological University, 50 Nanyang Avenue, Singapore 639798, Singapore

[‡]CNRS-International NTU Thales Research Alliance (CINTRA) UMI 3288, Research Techno Plaza, 50 Nanyang Drive, Singapore, Singapore 637553

[||] Temasek Laboratories@NTU, 50 Nanyang Avenue, Singapore 639798, Singapore

[#] School of Materials Science and Engineering, Nanyang Technological University, 50 Nanyang Avenue, Singapore 639798, Singapore

[$]Institute of Microelectronics, Agency for Science, Technology and Research (A*Star), 11 Science Park Road, Singapore 117685, Singapore

[*]Corresponding Author Email: HTTEO@ntu.edu.sg

KEYWORDS: three-dimensional graphene, three-dimensional h-BN, nano-thermal interface material, hot-spot removal, thermal management

ABSTRACT: Compression studies on three-dimensional foam-like graphene and h-BN (3D-C and 3D-BN) revealed their high cross-plane thermal conductivity (62 – 86 $Wm^{-1}K^{-1}$) and excellent surface conformity, characteristics essential for thermal management needs. Comparative studies to state-of-the-art materials and other materials currently under research for heat dissipation revealed 3D-foam's improved performance (20 – 30% improved cooling, temperature decrease by ΔT of 44 – 24°C).
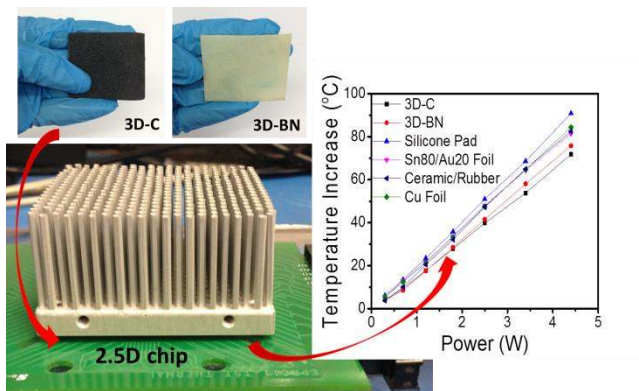
The advancement of semiconductor technology in the era of "more-than-Moore"[1] has led to an increasing challenge in thermal management. Integrated circuits (ICs) are so densely packed that they heat up within milliseconds,[2, 3] resulting in an extreme increase of generated heat[4] (*e.g.* current power electronics modules can go up to 200 Wcm^{-2}).[5] In order to mitigate this problem, the conventional way of extracting the heat out through the substrate has been improved *via* adding heat sinks either on top or below the electronic device. The contact to these heat sinks is further enhanced through thermal interface materials (TIMs)[2] and these TIMs are essential to reduce the thermal boundary resistance between the chip's active area and the heat sink.[6] Typical TIMs can be classified into electrically conductive and insulative types. For the former class, metal alloys containing In, Bi, Sn, Au are the common materials used. Although their thermal

conductivities are usually high (*i.e.* ~50 Wm^{-1}K^{-1}), the use of these TIMs is sometimes limited, due to their electrical conducting nature that can interfere with RF components and their limited integration ability with other-non-metal materials due to their wetting properties. Additionally, for miniaturization of devices, the TIMs utilized have to shrink in size and weight correspondingly as well. Thus only the use of very thin metal foil is allowed which decreases the effective thermal conductivity by several orders.[7] Also, the use of metallic TIMs require high temperatures for reflow in order to achieve good surface conformity, which can range between 90°C to 450°C limiting its usage.[8] For electrically insulating TIMs, typical materials include greases, phase change materials, gels, adhesives and polymers.[4, 9, 10] These TIMs are able to achieve good surface conformity at low temperature and are relatively easy to apply. Nevertheless, their thermal conductivities remain in the lower regime (0.1 – 0.3 Wm^{-1}K^{-1}).[4] Many have improved these materials by infiltrating with high thermally conducting fillers, such as metals (*i.e.* Ag, Au, Ni, Cu)[11] and ceramics (*i.e.* Al$_2$O$_3$, AlN, BN).[12, 13] This strategy increases the thermal conductivity of commercial available TIMs to 5 – 10 Wm^{-1}K^{-1}.[14] Despite this, this is still much lower than typical metallic TIMs and electronics materials, which creates a bottleneck in the thermal extraction channels (*i.e.* typical solder materials have a thermal conductivity ranging between 20 – 60 Wm^{-1}K^{-1} at room temperature).[15-17] Although one could increase the loading fraction of the fillers to increase the thermal conductivity, large filling ratios would also affect its viscosity and other parameters defining the applicability, such as curing temperature, dry-out and pump-out.

Today, the demand in performance for modern ICs has already pushed the current TIMs beyond their limit.[18] As a consequence, the performance of new generation chips has to be lowered at times to avoid over-heating[19] (which means adjusting their frequency according to the

temperature).[20] This is obviously undesirable.[21] As such, it is of importance to overcome this heat dissipation challenge[22] and many have begun to explore various nanomaterials as next generation nano-thermal interface materials.[23]

Recently, there has been a trend of up-scaling two-dimensional (2D) materials, such as graphene and h-BN, into freestanding 3D space.[24, 25] The obtained structures are of ultra-light weight (99.6% porosity, density of $1 - 5$ mg cm^{-3}), and have enhanced mechanical and surface area properties while keeping the well-reported 2D-structural properties.[26, 27] For the case of three-dimensional graphene (3D-C), studies have shown that it has comparatively high thermal conductivity, electrical conductivity, chemical/thermal stability and EMI shielding properties;[28-31] and for three-dimensional boron nitride (3D-BN), it has an equally high thermal conductivity but is an electrical insulator.[30] In addition, it has been reported that the interconnected nature within the 3D-foams could drastically overcome the internal contact thermal resistance, since single graphene domains within the 3D-foam form a continuous graphitic structure through covalent bonding.[28] It has been shown that such foam-like structures have superior thermal interfacial characteristics to other surfaces due to the increased contact surface area.[32] Furthermore, it has also been predicted that the current thermal conductivities can be further increased by increasing the density of the 3D-foams.[28] Therefore, it is believed that as the density of these foam-like materials increases, the overall thermal extraction performance would far exceed the thermal performance of the current TIMs.

Herein, we study the application of 3D-C and 3D-BN as an ideal electrical conductive and insulative TIM candidate, respectively, to overcome current thermal management challenges. For both of these high-density 3D-C and 3D-BN, characteristics that are critical to TIMs have been investigated, which include cross-plane thermal conductivities as high as $62 - 86$ Wm^{-1}K^{-1},

interface, thermal stability upwards of 700°C and, most importantly, evaluation of the thermal extraction efficiency on a state-of-the-art 2.5D electronic platform. Additionally, all results have been verified with commercial software COMSOL Multiphysics simulations.

Our results have shown an exceptional performance as TIMs with a drastic decrease of chip temperature on the 2.5D test platform from ca. 95°C to 51°C (ΔT° of 44°C) for 3D-C and to 71°C (ΔT° of 24°C) for 3D-BN at an applied power of ~5 W, which is 20% colder than any of the commercially available TIMs tested on the same platform (*i.e.* Sn/Au) and among the highest temperature decrease of hot spots on actual chips reported so far (*e.g.* highest values for alternative heat spreaders currently under research range around ΔT ~ 13°C for a CVD-graphene heat spreader,[26] ΔT ~ 6 – 12°C for a graphene-based film with added silane-functionalized molecules,[27] and ΔT ~ 20°C for exfoliated few-layer graphene).[33] This is a significant decrease, since it is known that the decrease of hot spot temperature on chips by 20°C extends the transistors lifetime by one order of magnitude.[33] It must be also noted that for most alternative materials currently under research, the cooling down of the hot spot is *via* the distribution of the heat throughout the film in the in-plane direction and not by extracting it upwards (to a heat sink). At equilibrium, such spreading of the heat would keep the entire chip at elevated temperatures and defeats the purpose of maintaining the chip below a safe operating region.[15] Contrastingly, for 3D-foams, their outstanding thermal conductivity in the cross-plane direction and their thin thickness (which will fasten up the heat transfer upwards, rather than lateral), makes them thus ideal candidates for solving current thermal management needs.

RESULTS AND DISCUSSION

A.   3D-foam fabrication and characterization

3D-foams were prepared with chemical vapor deposition (CVD) method on Ni template, as reported previously,[30] and the resulting structures are shown in **Figure 1**. Figure 1a and b show optical images of the pristine 3D-C and 3D-BN structures, respectively; Figure 1c shows a scanning electron microscopy (SEM) image of the cross-section of the 3D-foam. It can be seen that the pores have a mean diameter of $100 - 200$ µm, homogeneously distributed within the 3D-foam. The overall thickness of the 3D-foam is of ca. 1.7 mm with a porosity of 99.6% (corresponding to only 0.4% actual material, the rest being free space) and density of 1 mg cm^{-3} for the pristine 3D-BN and 5 mg cm^{-3} for pristine 3D-C. Figure 1d shows a transmission electron microscope (TEM) image taken at the edge of a 3D-foam pore. It can be seen that the structure of the 3D-foam comprises of stacked layers of graphene or h-BN, for the case of 3D-C and 3D-BN, respectively. Typical 3D-foam has between 8 and 10 layers. The number of layers can be tuned by the growth parameters; above 10 layers, the 3D-foam starts to resemble graphitic or bulk h-BN structures. To increase the density of the 3D-foams, two approaches have been used; namely, (1) prolong the growth duration and (2) by simply compressing the 3D-foam with an applied force, as depicted in the schematic of Figure 1e. The difference between the two is mainly that in (1), the thickness of the walls increases while the pore distribution remains unchanged. As for (2), it decreases the pore size but the thickness of the walls remains unchanged. To verify the quality of both 3D-foams, Raman spectroscopy was performed on both samples. The results show a stable quality throughout the varieties of 3D-foams. The typical peaks for a high quality multi-layer graphene, together with their ratio, are well preserved in all three graphs (G-peak at 1580 cm^{-1}, 2D-peak at 2700 cm^{-1}, absence of D-peak at 1350 cm^{-1} and a ratio of G:2D-peak intensity of 0.25).[34]

The electrical conductivity of the 3D-foams was measured with Van-der-Pauw method, 3D-BN has an electrical resistivity of 16.0×10^6 Ωcm and 3D-C has an electrical resistivity of 1.7 Ωcm.
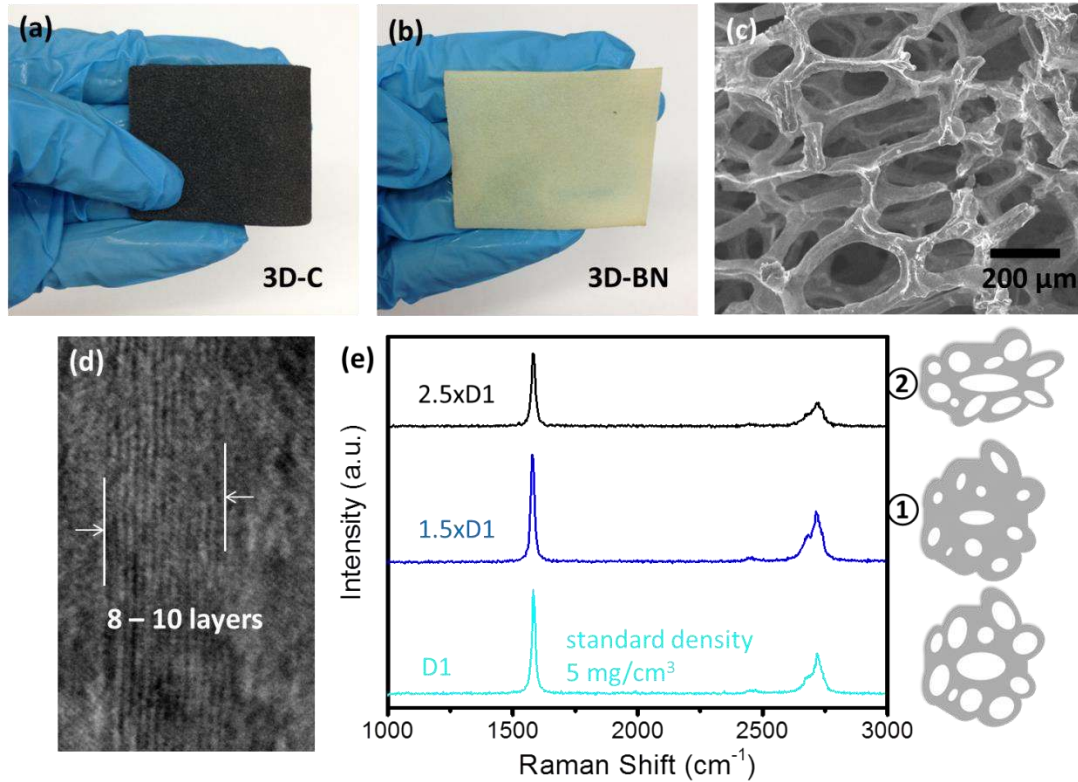
Figure 1. Material characterization of the 3D-foams. **(a)** Optical image of 3D-C; **(b)** optical image of 3D-BN; **(c)** SEM image of the cross-section of a typical uncompressed 3D-foam; **(d)** TEM image of the edge of a 3D-foam to determine the amount of layers comprising the 3D-foam; **(e)** Raman spectroscopy on the 3D-foams with different density obtained through the two different methods to increase layer numbers.

B. Thermal conductivity

As reported previously, the biggest constrain for the effective thermal conductivity of the 3D-foams is the very low volume fraction (0.4%),[28] hence, if the density of the 3D-foam could increase, the thermal conductivity will rise by several orders.[30]

To investigate the correlation between the density of the 3D-foams and their respective thermal conductivities, the cross-plane thermal conductivity was measured using the laser flash method[35]

7

since the z-plane heat spread is more crucial for the effectiveness of heat extraction for TIMs.[15, 36] Supporting experiments to proof the suitability of the laser flash technique for the porous 3D-foams is provided in the Supporting Information (**Figure S1**). **Figure 2**a and 2b show SEM images of two different 3D-foams with different density and it can be clearly observed that the size of the pores decreases accordingly. Figure 2a shows a sample 90 times denser than the standard sample. The branches and pores can still be clearly distinguished, while the spacing between individual pores reduces. Figure 2b shows the maximum density achievable, whereby all pores have been closed and only the outline of the walls are still visible.

Obtained thermal conductivity results are shown in Figure 2c, in which the thermal conductivity (red curve) was plotted along with its corresponding density (blue curve) for each measured sample. Closed squares represent results for 3D-C and open squares for 3D-BN. The base thermal conductivities of the pristine 3D-foams are of 1.2 $Wm^{-1}K^{-1}$ and 0.84 $Wm^{-1}K^{-1}$, for 3D-C and 3D-BN respectively. As the density increases, the highest thermal conductivity values achieved are at 86 ± 10 and 62 ± 10 $Wm^{-1}K^{-1}$ for 3D-C and 3D-BN (error deviation due to the non-perfect surface flatness), respectively. It must be noted that 3D-BN has a slightly lower thermal conductivity than 3D-C, due to the cumulative effect of the following structural differences: (1) h-BN and graphene have a different phonon dispersion, especially in their flexural modes (which in turn leads to increased phonon-phonon scattering),[37-39] (2) higher isotopic impurity in h-BN (i.e. BN has a larger isotope mixture of 19.9% ^{10}B and 80.1% ^{11}B than graphite with 98.9% ^{12}C and 1.1% ^{13}C, which leads to an increase in phonon-isotope scattering. This in turn reduces the thermal conductivity in BN),[39, 40] (3) the difference in mass of B and N (since the phonon frequency depends on the mass, and thus in BN local fluctuations in the natural frequency appear which leads to additional phonon scattering)[38, 41] and (4) intrinsic

phonon-phonon scattering due to lattice anharmonicity (also caused by the dual-character of BN, as compared to graphene).[39, 42]

The results show that there is a proportional relation between density and thermal conductivity for both types of 3D-foam. In addition, it is also worth mentioning that the two methods of obtaining high-density 3D-foam (*i.e.* prolong growth time and compression of the 3D-foam) have been compared and their thermal conductivities are comparable. The reason is that both these methods do not change the internal configuration of the 3D-foam and thus the internal thermal contact resistance remains low.[28]

The cross-plane thermal conductivities for 3D-C and 3D-BN increased 14-fold and 30-fold over typical multilayer graphene and h-BN (*i.e.* graphene has a thermal conductivity of 6 and h-BN of $1.5 – 2.5$ $Wm^{-1}K^{-1}$ in the z-plane).[43, 44] This is due to the isotropic interconnected structure of the 3D-foam: while in 2D graphene (or h-BN), phonon transport is anisotropic (*i.e.* only along the in-plane direction, and for out-of-plane propagation between the layers only weak Van der Waals forces are present which do not enable efficient phonon transport), in 3D-foams, the graphene or h-BN sheets are stitched to each other covalently and follow an isotropic structure, which is preserved even when density is increased. This way, in 3D-foams the phonon transport can be directed into all directions in an isotropic manner.
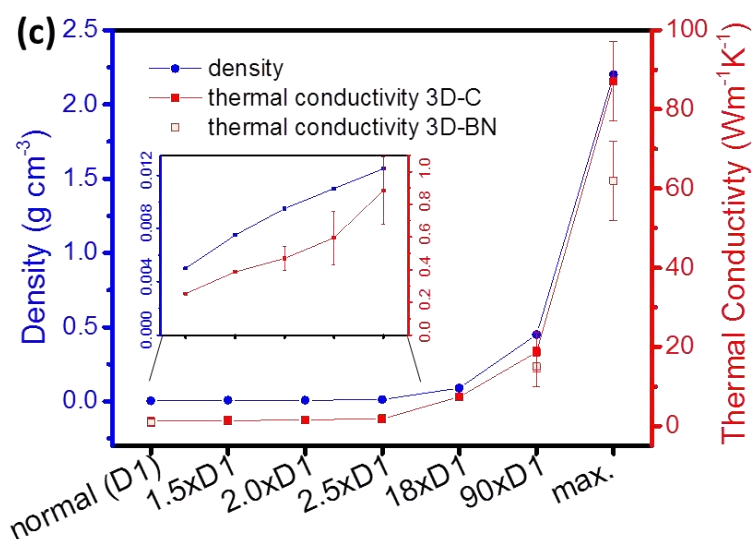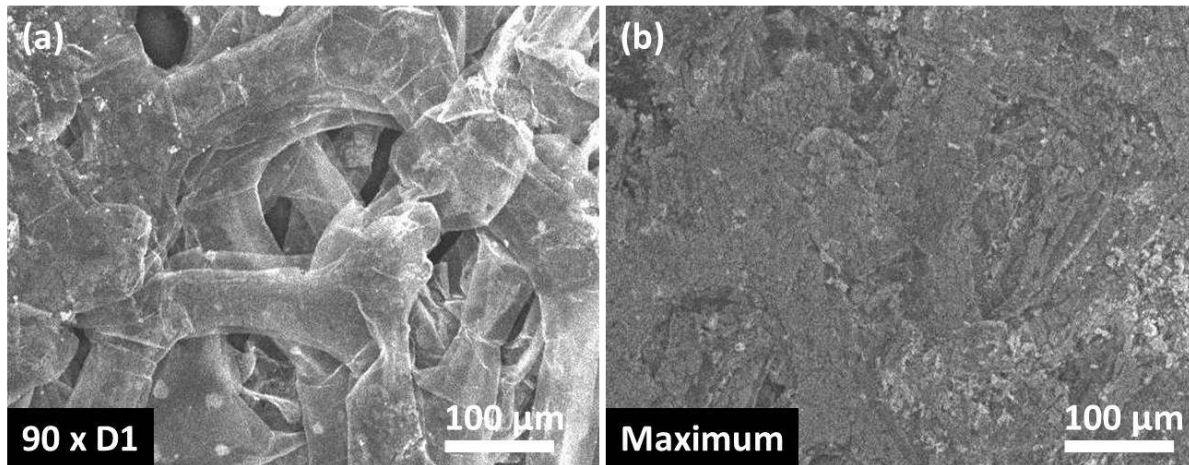
Figure 2. Study of thermal conductivity as a function of density. **(a)** SEM image of a 3D-foam compressed down to 90 times its original density D1, **(b)** SEM image of a maximum compressed 3D-foam; **(c)** measured density and thermal conductivity of 3D-C and 3D-BN (inset: zoom into the first 5 measurement points).

Also, these maximum values of thermal conductivity are among the highest cross-plane conductivities of free-standing graphene or h-BN structures. For comparison, the closest structure to the 3D-foams studied here is graphene and h-BN paper. For this type of structures, thermal conductivity in the out-of-plane direction is difficult to improve further due to the anisotropic behavior and alignment of the graphene or h-BN particles (maximum values reported are of $1 - 5$ $Wm^{-1}K^{-1}$).[45] This becomes very evident when observing their cross-sectional SEM

images, whereby the layered structure can be clearly seen.[46, 47] Further comparison to other structures is given in **Table 1**.

Table 1. Comparison of cross-plane thermal conductivities among graphene and h-BN structures

Material	Cross-plane thermal conductivity [W m^{-1}K^{-1}]	Remarks	Ref.
Graphene	6	Weak Van der Waals forces limit conductivity between layers	[44]
h-BN	1.5 – 2.5	Same as graphene	[43]
Graphene paper	max. 1 – 5	anisotropic behaviour and alignment of the G particles, which becomes evident in the layered structure under SEM	[45, 46]
h-BN paper/BN-polymer nanocomposites	n.a. (only in-plane)	Similar to G paper, h-BN paper is extremely layered Pure BN has weak strength and is difficult to obtain as freestanding film, thus needs support from another material	[47-50]
Commercial Silver epoxy TIM	1.76 (pristine) 9.9 (5 vol% graphene filler)	stable in working temp range of epoxy, which is only 5 – 75 °C	[16]
Graphene nanocomposite epoxy	5.1 (10 vol%)	Stable only at 5 – 75 °C	[36]
Graphene laminate on PET	40 – 90	Strongly dependent on flake size due to the amount of single flakes required not freestanding	[51]
Multilayer graphene in epoxy	5	Temperature dependence of values, not freestanding	[52]
3D BN nanosheet networks in epoxy	2.4 (9.29 vol%)	Infiltrated in epoxy anisotropic	[53]
h-BN in polyimide	7 (60 vol%)	Not freestanding and requires high volume fractions	[54]
3D-foam	62 ± 10 (BN) 86 ± 10 (C)	Freestanding and compressible, stable up to 700 – 900 °C	This work

Also, for actual application, it is challenging to obtain freestanding graphene or h-BN structures that can be applied directly without the need of supportive materials (such as polymers), which further hinders the phonon transport. For 3D-foams, besides their outstanding thermal conductivity, these 3D-foams do not require additional mixing with supporting materials and are fully freestanding.

C.   Interface characteristics

For TIMs, besides thermal conductivity, the quality of the interface with the chip and sink for heat dissipation plays a major role in the heat transfer. Some of the important considerations include: (1) thermal properties of the interface, (2) optimization of the interface, since due to the very bad conduction of heat in air (thermal conductivity of 0.026 $Wm^{-1}K^{-1}$ at room temperature) any presence of free space void in the joint area would increase the thermal resistance significantly, (3) surface roughness of the contact, (4) any possible stress occurring due to coefficient of thermal expansion (CTE) mismatches.[55] To investigate these interface properties, measurements according to ASTM5470 were performed.[56-60] The value obtained is of $R_{th} = 0.197$ KW^{-1} (0.262 in^2KW^{-1}), which is considered a very low thermal contact resistance. This is due to the very high surface conformity of the 3D-foam and shows that the 3D-foam is able to decrease the interface resistance of two mating surfaces. This value is in a similar range as in reported previously in a comparable test where 3D-C foam was placed between two Cu blocks (between Si and Al) and pressed down, which gave a thermal resistance of 0.45 KW^{-1} (0.26 KW^{-1}).[32] For comparison, the thermal interface resistance of commercial grease is around 6 times higher, at 2.71 KW^{-1}, and silicone based adhesive is 3 times higher, at 1.35 KW^{-1}.

To observe the morphology of compressed 3D-foam, Focused Ion Beam (FIB) and SEM have been used to measure the thickness of the branches of the 3D-foam and the 3D-foam itself after a compression step between two Si wafers. For this, a window has been cut through the compressed 3D-foam in order to access the 3D-foam within the sandwiched structure (**Figure 3**a). It can be seen that on average, each branch is between 1.1 and 1.3 μm thick (Figure 3b). Since the porosity of the Ni template used is between 100 and 110 ppi, and with an initial thickness of 1.67 mm of the 3D-foam, the number of vertical pores inside the structure is

between 6 and 7. Since samples comprised of 10 layers are used for this application, which are supposed to be non-compressible, then the minimum thickness the 3D-foam can reach is 6.6 μm. The SEM image also reveals that there is still free space present between the branches. This is due to the fact that there was a gap between the Si wafers due to its warpage,[61, 62] which is larger than the minimum thickness of the 3D-foam, thus the 3D-foam does not require full compressibility in order to fill this gap.

In order to quantify the compressibility of the 3D-foams, a study of the relationship between applied force and compression level is shown in **Figure S2**.

To further demonstrate that 3D-foam would fit into most surface roughness to improve the thermal interface, various artificial trenches of different aspect ratio were fabricated on a Si wafer as a test platform for extreme cases and compressed with the 3D-foam. The cross-section of the Si–3D-foam configuration was observed under SEM and Figure 3c-f show two examples of the trench-arrays before and after compression with the 3D-foam. Figure 3c,d show the case of 20 μm deep, 2 μm wide trenches; Figure 3e,f of the 40 μm deep and 25 μm wide section. For both cases, it can be seen clearly that the 3D-foam is able to completely fill up all the gaps. The good fitting of the 3D-foam into all the trenches is due to the fact that the structure of the 3D-foams is very refined and it is several orders smaller than the usual surface roughness or unevenness/warpage.
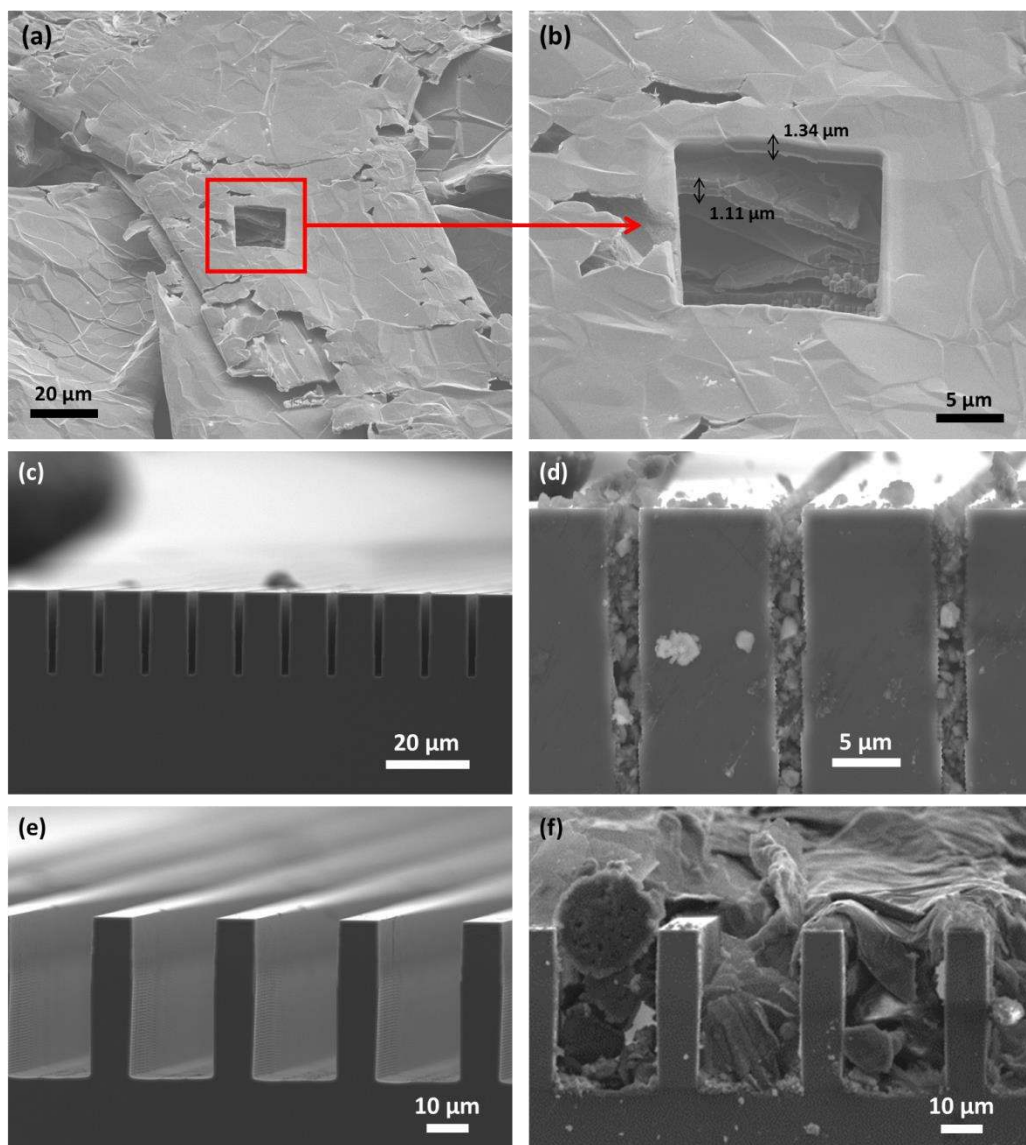
Figure 3. SEM studies of the 3D-foam after compression on varying surface roughness. **(a)** FIB cut has been performed to measure the thickness of the graphite inside the 3D-foam; **(b)** zoom into the cut with measurement; **(c)** cross-sectional view of the 20 µm deep and 2 µm wide trench before compression with 3D-foam and **(d)** after compression with 3D-foam; **(e)** cross-sectional view of the 40 µm deep and 25 µm wide trench before compression with 3D-foam and **(f)** after compression with 3D-foam.
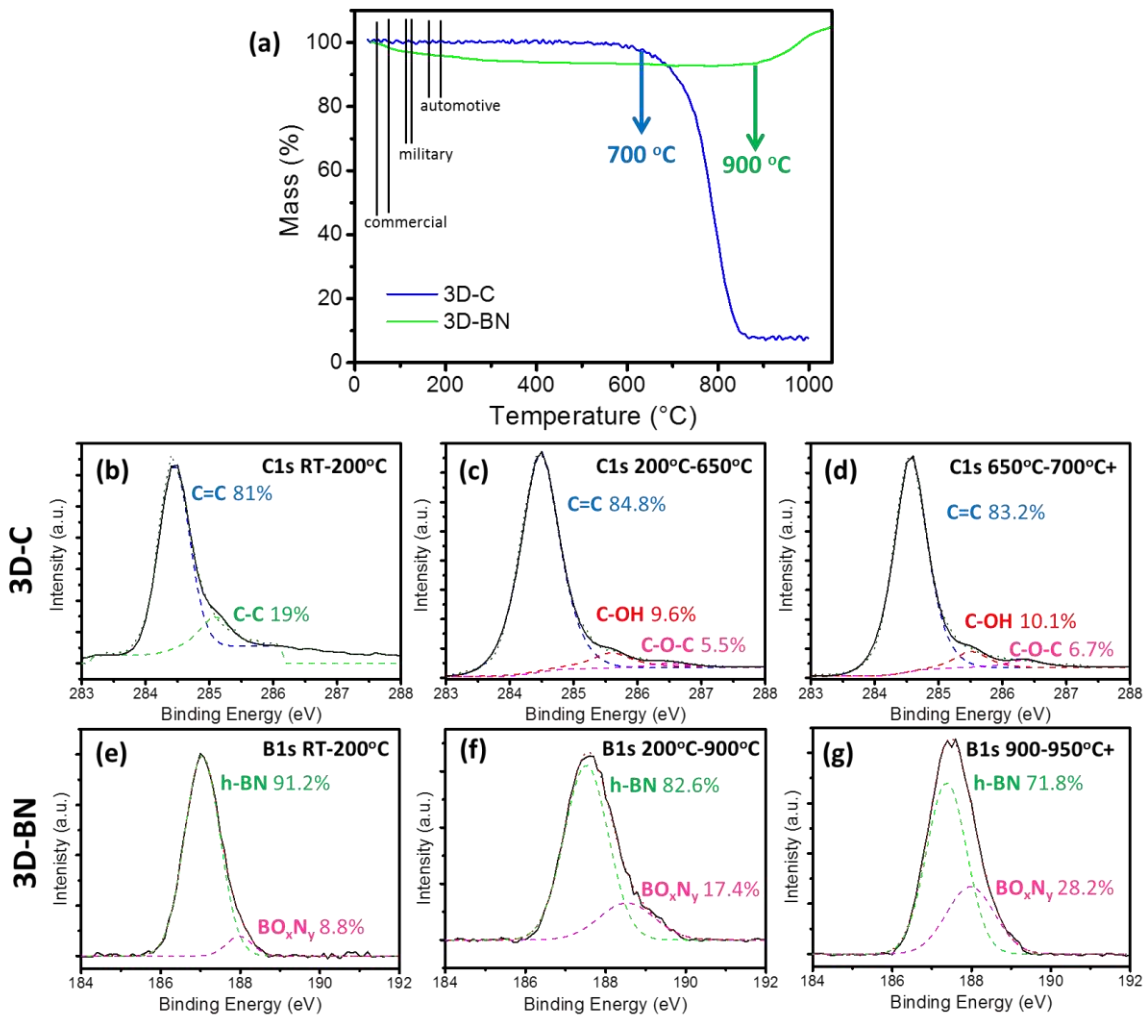
D.   Thermal stability

Thermal stability of the 3D-foams throughout a temperature range was assessed through thermogravimetric analysis (TGA). This method investigates the stability of the material at

elevated temperatures by heating them up to ~1100°C while monitoring their weight.[63, 64] Obtained curves are shown in **Figure 4**a, whereby the blue curve corresponds to 3D-C, which shows that 3D-C remains unchanged up to 700°C and that only after this point, it loses 95% of its weight; 3D-BN (green curve) on the other side remains stable up to 900°C, and then increases in weight, which is due to the oxidation of BN to B_2O_3 which is heavier in mass. The initial slight decrease of the 3D-BN mass is due to the loss of hygroscopic water.[65, 66] Both results are in good agreement with literature.[67, 68] It is worth mentioning that typical operating temperatures for electronics is of 65 – 85°C for commercial applications, 110 – 120°C for military electronic systems, and as high as 175°C for automotive ICs and the upper spectrum of military applications (all demarcated in the graph).[69] Evidently, both 3D-foams can withstand all the important operating temperature ranges. To ensure that the thermal conductivity of the 3D-foams remain stable throughout the temperature range of electronics, laser flash on uncompressed 3D-C was performed from room temperature to 200°C and **Figure S3** shows the obtained results. It can be seen that the thermal conductivity remains stable at ± 10%, which corresponds to previously reported values for this type of 3D-foam.[28, 30]

Besides TGA, X-ray Photoelectron Spectroscopy (XPS) was used to analyze the thermal stability of the chemical structure. XPS analysis was carried out on the 3D-foams after exposure to different temperatures in air for one hour from 200°C and up to 720 °C for 3D-C and 920°C for 3D-BN. The results are shown in Figure 4b-g. For the case of 3D-C, in the range of room temperature to 200°C, only pure graphitic structure was detected, comprising of only carbon aromatic groups. Starting at 200°C, an oxidation of 5 – 6% is visible, which only slightly increases at 700°C (*i.e.* the point of mass loss). For the case of BN, a similar behavior can be observed; BN oxidizes slightly with increasing temperature, but the level of oxidization remains

in a low regime of 8 – 17%. This very high thermal stability beyond the usual operating temperatures is of great advantage, especially for electronics, where the increase in both compactness and performance has generated thermal problems. In particular for electrically insulative TIMs, one of the current challenges is their thermal stability beyond temperatures of 120 – 200°C (*i.e.* polymers degrade under such high temperatures,[70] grease hardens).[1] 3D-foams (*i.e.* 3D-BN for electrically insulative TIM) on the other hand are capable to withstand the increasing demands for electronics in high temperature environment.

Figure 4. Thermal stability of the 3D-foams. **(a)** Measured *via* TGA curves of 3D-C (blue) and 3D-BN (green); and through **(b, c, d)** C1s XPS high resolution spectra of 3D-C at different

temperature ranges, **(e, f, g)** B1s XPS high resolution spectra of 3D-BN at different temperature ranges.

E.   Performance test in a 2.5D IC platform

To assess the heat extraction performance of 3D-foams on electronic devices, evaluation was carried out on a 2.5D electronic test platform.[71] 2.5D packages refer to the packaging of multiple dies on a Si interposer with Cu-filled Through Si Vias (TSVs) as electrical interconnects. Dissimilar dies with different functions can be assembled together to fulfill faster operation through shortened interconnects. Nevertheless, even though the shortened interconnect lengths reduce the power consumption, the power dissipation for each die tends to remain unchanged. This results in unfavorable heat density within the packages. Thus, thermal management is a key challenge to be addressed in 2.5D packages and system designs,[72, 73] whereby the TIMs performance can play a key role in 2.5D packages cooling.

Figure 5a shows a photograph of the setup used, in which the 3D-foam is compressed directly between the test chip and the heat sink (marked here with an arrow). Also for this setup, the 3D-foams were first placed in their uncompressed state onto the chip and then compressed down *via* the weight of the heat sink. Two types of test chip where used, one where the heating element is exposed (denominated as "no overmold", Figure 5b) and another where the heating source is covered with a mold (denominated as "with overmold", Figure 5c). The difference between the two is that in the former case, the performance only depends on the material itself (thus a direct evaluation of the heat spreading capabilities of the material), whereby for the latter, it is a more application-related situation where the performance is also affected by the low conducting overmold material, since the heat has to first go through it before being transferred to the TIM and then the heat sink. As such, measurement with overmold would result in an overall reduction

17

of the heat extraction performance. A more detailed description of the test chip can be found in the Experimental Section and a schematic and photograph of the system without any overmold are shown in **Figure S4**. In brief, a thermal test die is placed on a Si interposer, together with two dummy dies, which represent the logic and memory chips in a typical 2.5D integration. The voltage of the thermal test die is gradually ramped up, while an internal diode voltage (which detects the temperature increase in the chip) is recorded. With this, the temperature at the chip's junction to ambient can be deduced.

Besides the 3D-foams, other standard TIMs were evaluated in order to benchmark the performance. Figure 5d shows the obtained results, 3D-BN is being compared directly with other electrically non-conducting TIMs and 3D-C with other electrically conducting TIMs.

The graphs show the increase in temperature at the junction of the chip to the ambient as a function of applied power. All materials tested have a linear relation. Only the gradients change between the materials.
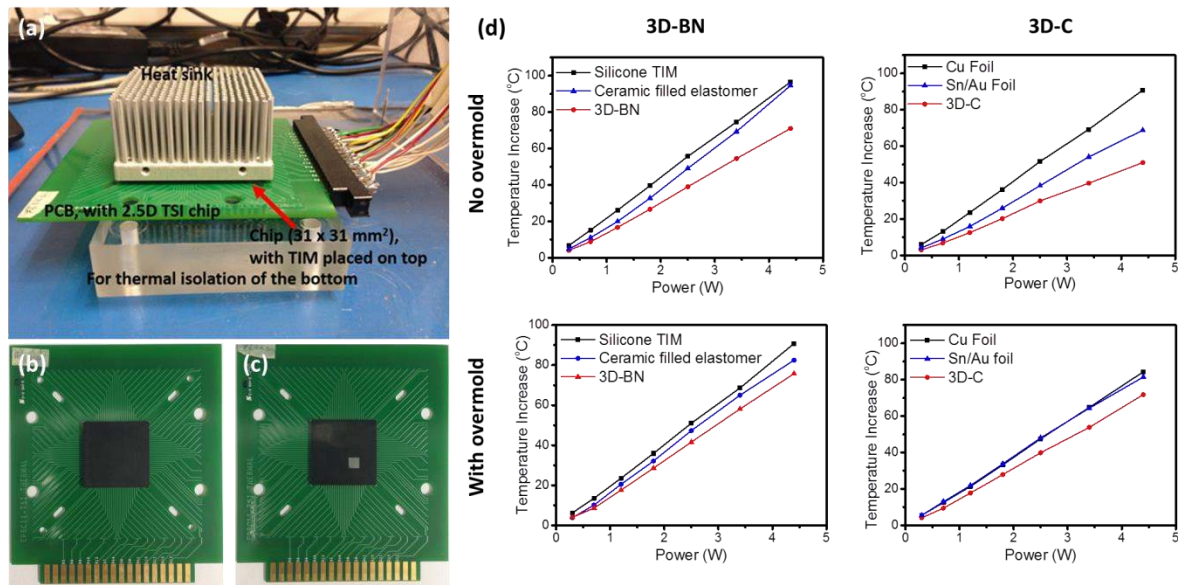
Figure 5. Test on field. **(a)** 2.5D test setup used; **(b, c)** top view of the chip used, with and without overmold on the heater section; **(d)** obtained results, grouped according to device used and electrical conductivity characteristic, mean error deviation ±0.19˚C.

Comparison of the curves shows that the 3D-foams perform with higher efficiency: the measured change in temperature of the chip shows that 3D-foams are able to maintain the device at a lower operating temperature. The slopes of the graphs are enlisted in **Table 3** together with the achieved improvement over the standard TIMs tested. It can be seen that in all these cases, the 3D-foams achieve a significant decrease in its temperature differential; for instance, 3D-BN is able to maintain the chip 10% and 25% cooler than its commercial electrically insulating counterparts with and without overmold, respectively (this is equivalent to 15.06°C and 23.6°C less heat at the point of maximum power applied during the test), and 3D-C achieves 12% and 42% improvement over its electrically conducting counterparts, equivalent to 12.56°C and 39.85°C less heat at 4.4W, for the overmold and non-overmold case, respectively.

Table 3. Temperature increase slopes for various materials tested with the 2.5D platform

		Material	Slope [°C W^{-1}]	Improvement [%]
No overmold	Electrically insulating	3D-BN	16.6	-
		Silicone TIM	22	25
		Ceramic filled elastomer	22	25
	Electrically conducting	3D-C	12	-
		Cu-foil	16.2	26
		Sn/Au-foil	20.8	42
With overmold	Electrically insulating	3D-BN	17.8	-
		Silicone TIM	19.6	10
		Ceramic filled elastomer	20.6	14
	Electrically conducting	3D-C	16.6	-
		Cu-foil	18.8	12
		Sn/Au-foil	18.8	12

Table 4 compares the obtained results with values reported by other thermal management materials tested on different test-platforms from literature. It must be noted that the reported values in these examples were obtained without the use of overmold on top of the hot spot. It can be seen that for such cases, the 3D-foams outperform other materials, paired with better applicability (*e.g.* one of the alternative approaches which achieved the highest temperature decrease of 20°C, using exfoliated graphene quilts,[33] is still 4°C lower than 3D-BN and 24°C lower than 3D-C, and it requires a precise control over layer number, exfoliated size and location, which is difficult to achieve).

Table 4. Comparison of hot spot temperature decrease of different materials

| Material	Achieved temperature decrease of hot spot	Remarks	Test platform	Ref.
CVD-Graphene heat spreader	ΔT~ 13°C at 0.0156 to 0.624 W	Application of graphene not very practical (requires PMMA transfer to platform, then hot acetone to remove PMMA)	Pt micro-heater, temperature determined from measured resistance	[26]
Graphene paper	ΔT ~ 24-18°C (from thermal camera image)	Orientation of films only parallel to platform	Samples suspended above an iron head, temperature recorded through IR camera	[46]
Exfoliated graphene quilts (few-layer graphene)	ΔT = 20°C[b]	Layer number, exfoliated size and location are difficult to control through exfoliation	AlGaN/GaN HFETs, ΔT determined from temperature-dependent shifts in Raman peak positions	[33]
Layered h-BN film	ΔT = 20°C	Not freestanding, requires acetate cellulose support, polycrystalline BN	Micro-heater configuration, temperature recorded through IR camera	[74]
Graphene-based film with addition of silane-functionalized molecules	ΔT ~ 6-12°C[b] at 2.52 W	Material only oriented in parallel	Pt micro-heater, temperature determined from measured resistance	[27]
3D-foam	ΔT ~ 15°C[a)b)]/24°C[b] (3D-BN) ΔT ~ 23°C[a)b)]/40°C[b] (3D-C) at 4.4 W	Orientation of structure isotropic, improved thermal conductivity out of plane, thus heat is extracted, rather than spread along the film	Thermal test die, temperature determined through internal diode voltage	This work

[a]Use of overmold on top of the hot-spot
[b]Use of heat sink on top of the hot-spot

Also, similarly to the 3-layer laser flash measurement, the compression with the heat sinks is sufficient to compress down the 3D-foam to conform to the surface profile, but it does not yield maximum compression. Nevertheless, this is sufficient enough to obtain enhancement of heat extraction.

Besides showing the outstanding performance of the 3D-foams, these results also highlight that heat-spreading performance not only depends on the thermal conductivity of the material used, but also on the surface conformity. For example, the metal foil's performance was comparable to the ceramic filled elastomer, even though their thermal conductivities differ by more than 50 $Wm^{-1}K^{-1}$ (*i.e.* the thermal conductivity of the elastomer is of 3.3 $Wm^{-1}K^{-1}$, Sn/Au foil is of 57 $Wm^{-1}K^{-1}$).

Moreover, since the purpose of the TIM is to displace any micro and/or macroscopic free space voids in between interfaces to improve heat conduction, any inclusions beyond the size of these gaps would be redundant and eventually lower the overall interface thermal conductivity. To further analyze the correlation between surface roughness and the optimized thickness for TIMs, tests with 3D-foams of varying thickness were performed on the mold and heat sink with different surface roughness and the results are summarized in **Figure 6.**
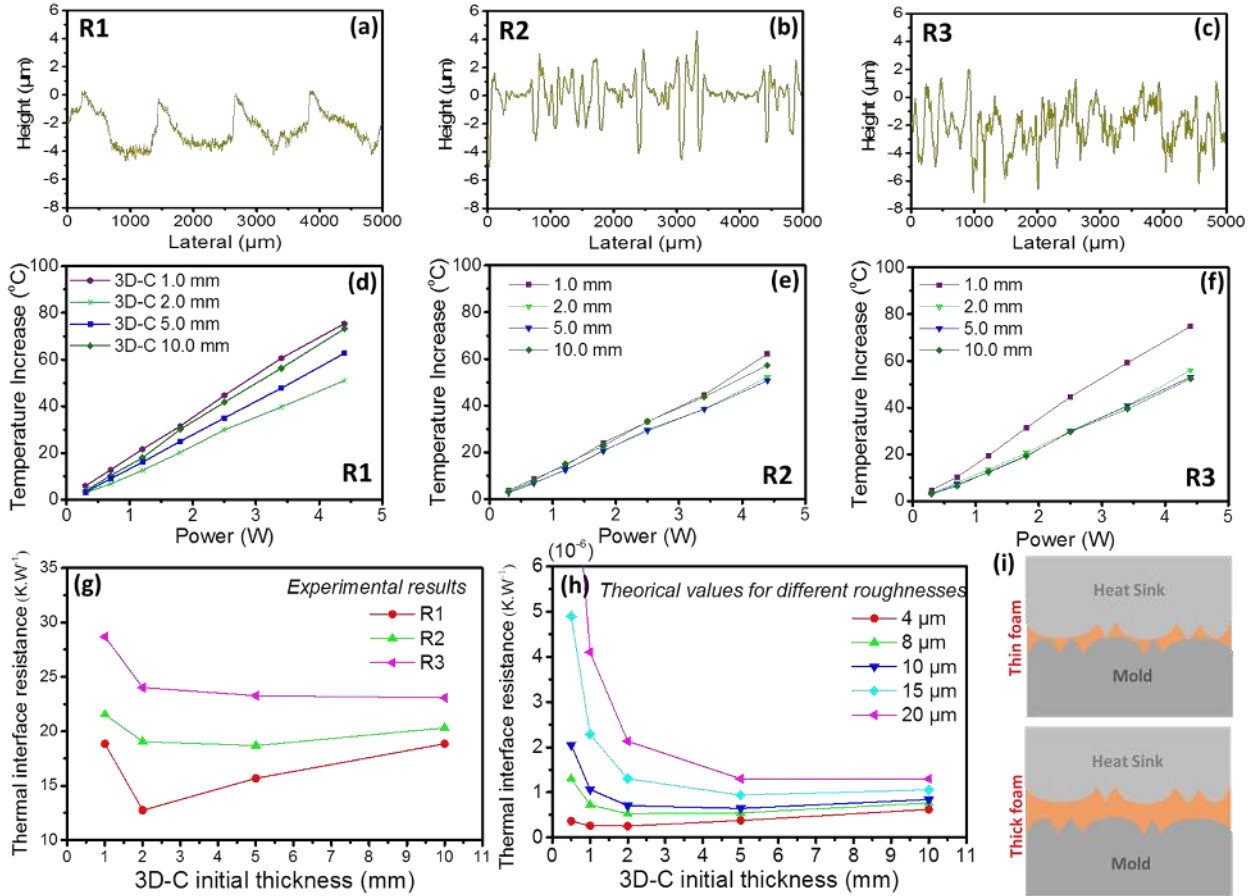
Figure 6. Delta surface roughness. **(a, b, c)** surface roughness profile of the three heat sinks used; **(d, e, f)** corresponding results obtained using the test setup from Figure 5, mean error deviation ±0.21˚C. **(g)** Experimental results for different surface roughness measured at 4 W as a function of starting thickness of the 3D-foam; **(h)** theoretical results for different surface roughness and trend of the temperature increase measured at 4 W; **(i)** schematics of the use of 3D-foams as TIM with different starting thickness.

The same setup of Figure 5 was used, with heat sinks of different surface roughness, namely R1, R2 and R3 being applied. A total of three heat sinks (the surface profile of each heat sink is shown in Figure 6a-c) were tested and for each heat sink, 4 different initial thicknesses of 3D-C were tested (*i.e.* initial thickness of 1 mm, 2 mm, 5 mm and 10 mm before being compressed and conformed to the interface)

Figure 6d-f shows the obtained graphs of temperature increase and Figure 6g shows the obtained results plotted as a function of initial thickness of the 3D-foam. Interestingly, it can be

seen that an initial thickness of 2 mm is enough for all cases to achieve an effective heat extraction (*i.e.* in the most roughened heat sink, the 2 mm result is nearly identical with the 5 mm and 10 mm result).

This can be explained as follows: as mentioned previously, the 3D-foam will fill all free space gaps between the mold and the heat sink. The resistance of the interface is thus the bulk resistance of the 3D-foam R_{3D} given by:

$$R_{3D} = \frac{t_e}{k_{3D}(t_e)} \tag{1}$$

where t_e is the effective thickness of the 3D-foam between the heat sink and the mold, k_{3D} is the thermal conductivity of the 3D-foam which is also dependent on the effective thickness. The Bruggeman assumption gives the relation between the thermal conductivity and the porosity, which also depends on the thickness.[75]

$$k_{3D} = k_G(1 - f(t_e))^{3/2} \tag{2}$$

with f the porosity and k_G the thermal conductivity of bulk 3D-foam (*i.e.* 86 Wm^{-1}K^{-1} according to the value obtained previously at maximum compression). When the heat sink compresses the 3D-foam on the mold, it fills all the free space gaps between the two mating surfaces; however, unlike the previous case with Si–Si, the mold is soft and will compensate for the non-flatness of the heat sink, which means that the thermal interface resistance is only affected by the surface roughness and the minimum thickness of the 3D-foam t_{min}. Due to this, it is possible to correlate the impact of the 3D-foam's effective thickness with the behavior of the thermal resistance for a given surface roughness: by combining relations (1) and (2), the calculation of the thermal resistance of the interface is computed in Figure 6h according to the initial 3D-foam thickness for 5 different roughness t_r (4, 8, 10, 15, 20 μm). The values of the effective thickness $t_e = t_{min} +$

t_r (addition of the minimum thickness reachable by the film with the surface roughness) used are summarized in **Table S1**.

   With this relation, it can be observed that for very thin thickness the thermal resistance is very high, which then continues to decrease until an optimal thickness is reached. This optimal thickness point is schematized in Figure 6i top and **Figure S5**, whereby the 3D-foam nicely fills in the free space gaps without creating any additional spacing between the heat sink and the mold (thickness/gap width $\delta \approx 0$). This optimal value is achieved with an initial thickness of 2 mm for the three cases of surface roughness tested here. Beyond this optimal thickness, compression of thicker 3D-foams leads to two simultaneous effects, namely the compression of material at the edge of the grooves (which leads to the addition of extra-material between the two mating surfaces, depicted in Figure 6i bottom, $\delta \gg 0$) and to a higher compression level of the 3D-foam inside the gap (as can be seen through comparison of the SEM images in Figure S5). Since a higher compression level inside the grooves leads to lowered thermal interface resistance, but at the same time the addition of material between the surfaces increases it, the two opposing effects sum up to an overall less linear increase of thermal interface resistance. This becomes evident in the case for R2, where the 5 mm 3D-foam achieves a similar performance as the 2 mm 3D-foam, since the slight addition of extra material between the surfaces is balanced off with an increased level of compression inside the gaps. The same applies to the case for R3 sample with the 10 mm thick 3D-foam. This is why in Figure 6g and 6h, the 2 mm 3D-foam achieves optimal thermal interface resistance results up to a surface roughness of 10 um and slightly thicker 3D-foams do not change this performance. It must be noted that experimental and theoretical values match, and the optimal thickness for each surface roughness can be reliably predicted.

CONCLUSION

In this work, high-density 3D-foams were studied for use as high-performance TIMs. Results have shown that high thermal conductivities across the plane direction in the range of 62 – 86 $Wm^{-1}K^{-1}$ were achieved, which is a 14- and 30-fold increase towards their 2D counterparts, 300-800 times higher than standard TIMs and a 10-fold increase over recent reported TIMs that are comprised of other nanomaterials (such as graphene laminate, graphene and h-BN paper). In addition, due to the compressible nature of the 3D-foams, a superior surface conformity was revealed. It has also been shown that the materials can withstand temperatures up to 700 – 900°C without any chemical changes, which is at least 500°C above current available TIMs. Direct comparison of the 3D-foams to other state-of-the-art TIMs has shown improved cooling performance by 20 – 30%, and comparison to other results from literature also revealed the superior qualities of the 3D-foams. In addition, for optimum performance, it has also been shown that for TIMs, it is important to match its thickness to the size of the free space void in between as any thickness beyond this limit would eventually increase the thermal interface resistance. This optimization has been demonstrated for the 3D-foams through combined simulation and experimental results. These overall enhancements in thermal performance are due to the isotropic thermal behavior given by the initial foam-like, interconnected structure, which is contrasting to usual nano-TIMs, where only weak Van der Waals forces ensure the contact between layers, and thus hindering good phonon transport.

Besides its high cross-plane thermal conductivity and excellent surface conformity, the herein presented 3D-foams are of a free-standing material that can be applied directly at room temperature without any need for reflow or curing. Together with their availability in both electrically conducting and insulating mode, these 3D-foams combine the advantages of both

metallic TIMs (*i.e.* high thermal conductivity) and polymeric/adhesive-based TIMs (*i.e.* good surface conformity). These advantages would allow electronics to be driven towards a higher power regime and enable a closed-form solution[15] for future electronics device package.

EXPERIMENTAL

Preparation of 3D-foams. "Growth of 3D-BN and 3D-C was carried out in a split tube furnace using Ni foam (Latech Scientific Supply Pte. Ltd.) as a catalytic substrate. For BN, 0.5 g of ammonia borane (NH_3-BH_3) is placed in a ceramic boat away from the heating element in the quartz tube. The Ni foam is annealed for 2 hours at 1000°C at low pressure (50 Pa), under H_2 flow, and is subsequently followed by BN growth which is initiated by heating the ammonia borane at 120°C, and the pressure is kept constant at 60 Pa. The growth for 3D-C was carried out similarly, with CH_4 as the C precursor gas (and shorter annealing of 5 minutes only). After growth, the lid of the furnace is lifted for fast cooling. The as-grown 3D-BN/C/Ni sample is dip coated with poly(methyl methacrylate) (PMMA) to protect the BN/C layers and then immersed into hot diluted hydrochloric acid (HCl) for at least 5 hours until the Ni is completely etched away. Finally, to remove the PMMA coating, the samples are annealed at 700 °C for 1 hour (in air for the case of 3D-BN and in Ar and H_2 environment for 3D-C)."[30]

Measurements. "SEM images were recorded with a JEOL JSM 5600LV at 15 keV, Raman spectroscopy (WITec CRM200 Raman with an Nd:YAG 532 nm laser as excitation source) was performed at room temperature to determine the crystalline configuration of the films. Thermal conductivity measurements were performed using the Laser Flash technique (LINSEIS XFA 500) at room temperature by first measuring thermal diffusivity α (mm^2s^{-1}).[76] Based on these results, the thermal conductivity κ ($Wm^{-1}K^{-1}$) can be calculated through Formula (3):

$$\alpha(T) = \frac{\kappa(T)}{c_P(T) \cdot \rho}$$

<div align="right">(3)</div>

where c_p (kJ kg^{-1}K^{-1}) is specific heat and ρ (kg m^{-3}) reference density at room temperature."[31] The error deviation was calculated by measuring 5 different spot locations on each sample. To ensure the correctness and repeatability of the last (fully compressed) sample, another set of 5 measurements was carried out on a second sample (i.e. a total of 10 measurements on 2 different samples for the fully compressed case). Specific heat was measured prior to the laser flash measurement using differential scanning calorimetry (DSC Q100, TA Instruments). The mass density was obtained by weighing a sample of known dimensions with a precision electronic balance (Mettler Toledo). The thermal conductivity is in cross-plane, meaning that it goes through the thickness-direction of the film. Electrical conductivity was performed using the Van-der-Pauw method on a four-probe Karl SUSS 200 Micro-Prober. Long term stability measurements were performed via TGA (DTG-60H, in air environment at 50 ml min^{-1}) and XPS (Thermo scientific theta probe XPS). Measurements of thermal contact resistance are conducted according to ASTM 5470 using a commercial system (AnalysisTech TIM Tester model 1400). The principle of this method is based on imposing a one-dimensional heat flow across the sample and measure the resulting temperature difference. The sample thermal resistance, R_{th}, is then defined as the ratio of the temperature difference to the heat flow. According to the Standard, the 3D-foams are considered Type II materials (low contact resistances, elastic and plastic deformations combined with an elasticity increase with deformation), so a controlled contact pressure is applied. Sample size is of 33 mm diameter disks, test temperature is of 50°C. Used pressure is of 10 psi, which yields full compression.

Test on field. "A thermal test die (5.08 mm × 5.08 mm) consisting of four heating unit cells, covering over 85% of the chip area to provide uniform heating, and six diodes for die temperature sensing, was fabricated onto a Si interposer (18 mm × 18 mm × 0.1 mm) together with two dummy dies (7.6 mm × 10.9 mm and 8 mm × 8 mm), which represent the logic and memory chips in a typical TSI integration. All the dies were fabricated and assembled on the same interposer wafer through microbumps and underfill processes. The interposer was then assembled onto an organic substrate (31 mm × 31 mm × 1 mm). For the molded packages, additional molding process was conducted on the wafer level to form the epoxy molded encapsulation on the chip package. A D-type edge connector was used to connect the thermal test chip to the power supply and diodes for thermal testing. The thermal diodes were calibrated in the air-convection oven with data taken at room temperature, 60°C, 100°C, and 140°C to obtain the proportionality factor (K factor in semiconductor thermal management). The six diodes on the thermal test chip have excellent linearity with R-squared value ≥ 0.9999, with almost identical K factor of 517 KV^{-1} ±1.2 KV^{-1} based on four calibrated packages on board. During the test, a power supply from Xantrex (XHR 150-7) was used to supply electrical power to the thermal chip, whereas the temperature reading was attained by activating the diodes with 1 mA current from the Keithley 2400 sourcemeter. For temperature increase test, the package was first placed in still air for 10 – 15 minutes without power input and then the diode voltage (V_{diode}) and the ambient temperature ($T_{a,0}$) were recorded as initial readings. A J-type thermocouple with factory calibration was used to measure the ambient temperature. The power input was then applied, and the corresponding junction temperatures and ambient temperature were recorded after reaching thermal equilibrium. The corresponding junction Temperature T_J was then calculated as follows:

$$T_J = \Delta V \cdot K + T_{a,0}$$

(4)

where $T_{a,0}$ is the ambient temperature before the power is input and ΔV the average of the diode

voltage difference before the power input."[71, 77]

ASSOCIATED CONTENT

Supporting Information. Figures S1 – S5, Table S1. This material is available free of charge

via the Internet at http://pubs.acs.org.

AUTHOR INFORMATION

Corresponding Author

*E-mail: HTTEO@ntu.edu.sg

ACKNOWLEDGMENT

REFERENCES

1.   http://www.businesswire.com/news/home/20151216005646/en/IDTechEx-Research-More-than-Moore-electronics-packaging, retrieved 16 December 2015
2.   Tong, X. C., *Advanced materials for thermal management of electronic packaging*. Springer Science & Business Media: 2011; Vol. 30.
3.   Viswanath, R.; Wakharkar, V.; Watwe, A.; Lebonheur, V. *Intel Technology Journal Q3* **2000**.
4.   Prasher, R. *Proc. IEEE* **2006,** 94, 1571-1586.
5.   Schulz, M., The Challenging Task of Thermal Management. In *PCIM, Nürnberg 2011*, 2011.
6.   Prasher, R.; Chiu, C.-P., Thermal Interface Materials. In *Materials for Advanced Packaging*, Lu, D.; Wong, C. P., Eds. Springer US: 2009; pp 437-458.
7.   Nath, P.; Chopra, K. *Thin Solid Films* **1974,** 20, 53-62.
8.   Green, R. E., *Machinery's handbook*. Industrial Press: 1992; Vol. 24.

9.   Farhad, S.; Whalley, D. C.; Conway, P. P. In *Thermal Interface Materials - A Review of the State of the Art*, Electronics Systemintegration Technology Conference, 2006. 1st, 5-7 Sept. 2006, 2006; pp 1292-1302.

10.   Liu, J.; Michel, B.; Rencz, M.; Tantolin, C.; Sarno, C.; Miessner, R.; Schuett, K.-V.; Tang, X.; Demoustier, S.; Ziaei, A. In *Recent progress of thermal interface material research-an overview*, Thermal Inveatigation of ICs and Systems, 2008. THERMINIC 2008. 14th International Workshop on, 2008; IEEE: pp 156-162.

11.   Li, Y.; Wong, C. P. *Mater. Sci. Eng. R Rep.* **2006,** 51, 1-35.

12.   Fu, J.; Shi, L.; Zhang, D.; Zhong, Q.; Chen, Y. *Polym. Eng. Sci.* **2010,** 50, 1809-1819.

13.   Zhu, B.; Ma, J.; Wu, J.; Yung, K.; Xie, C. *J. Appl. Polym. Sci.* **2010,** 118, 2754-2764.

14.   Huang, X.; Jiang, P.; Tanaka, T. *IEEE Elect. Insul. Mag.* **2011,** 27, 8-16.

15.   Moore, A. L.; Shi, L. *Mater. Today* **2014,** 17, 163-174.

16.   Goyal, V.; Balandin, A. A. *Appl. Phys. Lett.* **2012,** 100, 073113.

17.   King, J., *Materials handbook for hybrid microelectronics*. Artech House Inc: 685 Canton Street, Norwood, Massachusetts 02062, USA, 1988.

18.   Garimella, S. V.; Singhal, V.; Dong, L. *Proc. IEEE* **2006,** 94, 1534-1548.

19.   http://www.extremetech.com/extreme/222590-an-end-to-scaling-intels-next-generation-chips-will-sacrifice-speed-to-reduce-power, retrieved 20th May 2016

20.   https://www.pugetsystems.com/labs/articles/Impact-of-Temperature-on-Intel-CPU-Performance-606/ , retrieved 20th May 2016

21.   http://www.anandtech.com/show/9550/understanding-intels-dynamic-power-and-thermal-framework-smarter-throttling, retrieved 20th May 2016

22.   Garimella, S. V.; Fleischer, A. S.; Murthy, J. Y.; Keshavarzi, A.; Prasher, R.; Patel, C.; Bhavnani, S. H.; Venkatasubramanian, R.; Mahajan, R.; Joshi, Y. *IEEE Trans. Compon. Packag. Technol.* **2008,** 31, 801-815.

23.   Bar-Cohen, A.; Matin, K.; Narumanchi, S. *J. Electron. Packag.* **2015,** 137, 040803.

24.   Chen, Z.; Ren, W.; Gao, L.; Liu, B.; Pei, S.; Cheng, H.-M. *Nat. Mater.* **2011,** 10, 424-428.

25.   Yin, J.; Li, X.; Zhou, J.; Guo, W. *Nano Lett.* **2013,** 13, 3232-3236.

26.   Gao, Z.; Zhang, Y.; Fu, Y.; Yuen, M. M.; Liu, J. *Carbon* **2013,** 61, 342-348.

27.   Zhang, Y.; Han, H.; Wang, N.; Zhang, P.; Fu, Y.; Murugesan, M.; Edwards, M.; Jeppson, K.; Volz, S.; Liu, J. *Adv. Funct. Mater.* **2015,** 25, 4430-4435.

28.   Pettes, M. T.; Ji, H.; Ruoff, R. S.; Shi, L. *Nano Lett.* **2012,** 12, 2959-2964.

29.   Chen, Z.; Xu, C.; Ma, C.; Ren, W.; Cheng, H.-M. *Adv. Mater.* **2013,** 25, 1296-1300.

30.   Loeblein, M.; Tay, R. Y.; Tsang, S. H.; Ng, W. B.; Teo, E. H. T. *Small* **2014,** 10, 2992-2999.

31.   Loeblein, M.; Bolker, A.; Tsang, S. H.; Atar, N.; Uzan-Saguy, C.; Verker, R.; Gouzman, I.; Grossman, E.; Teo, E. H. T. *Small* **2015,** 11, 6425-6434.

32.   Zhang, X. F.; Yeung, K. K.; Gao, Z. L.; Li, J. K.; Sun, H. Y.; Xu, H. S.; Zhang, K.; Zhang, M.; Chen, Z. B.; Yuen, M. M. F.; Yang, S. H. *Carbon* **2014,** 66, 201-209.

33.   Yan, Z.; Liu, G.; Khan, J. M.; Balandin, A. A. *Nat. Commun.* **2012,** 3, 827.

34.   Ferrari, A. C.; Meyer, J. C.; Scardaci, V.; Casiraghi, C.; Lazzeri, M.; Mauri, F.; Piscanec, S.; Jiang, D.; Novoselov, K. S.; Roth, S.; Geim, A. K. *Phys. Rev. Lett.* **2006,** 97, 187401.

35.   Lim, K.-H.; Kim, S.-K.; Chung, M.-K. *Thermochim. Acta* **2009,** 494, 71-79.

36.   Shahil, K. M.; Balandin, A. A. *Nano Lett.* **2012,** 12, 861-867.

37.   Nag, A.; Raidongia, K.; Hembram, K. P. S. S.; Datta, R.; Waghmare, U. V.; Rao, C. N. R. *ACS Nano* **2010,** 4, 1539-1544.

38.   Sevik, C.; Kinaci, A.; Haskins, J. B.; Çağın, T. *Phys. Rev. B: Condens. Matter* **2011,** 84, 085409.

39.   Lindsay, L.; Broido, D. *Phys. Rev. B: Condens. Matter* **2011,** 84, 155421.

40.   Sevik, C.; Kinaci, A.; Haskins, J. B.; Çağın, T. *Phys. Rev. B: Condens. Matter* **2012,** 86, 075403.

41.   Che, J.; Çağın, T.; Deng, W.; Goddard III, W. A. *J. Chem. Phys.* **2000,** 113, 6888-6900.

42.   Sichel, E.; Miller, R.; Abrahams, M.; Buiocchi, C. *Phys. Rev. B: Condens. Matter* **1976,** 13, 4607.

43.   Simpson, A.; Stuckes, A. *J. Phys. C: Solid State Phys.* **1971,** 4, 1710.

44.   Delhaes, P., *Graphite and precursors*. CRC Press: 2000; Vol. 1.

45.   Wu, H.; Drzal, L. T. *Carbon* **2012,** 50, 1135-1145.

46.   Xin, G.; Sun, H.; Hu, T.; Fard, H. R.; Sun, X.; Koratkar, N.; Borca-Tasciuc, T.; Lian, J. *Adv. Mater.* **2014,** 26, 4521-4526.

47.   Zhu, H.; Li, Y.; Fang, Z.; Xu, J.; Cao, F.; Wan, J.; Preston, C.; Yang, B.; Hu, L. *ACS Nano* **2014,** 8, 3606-3613.

48.   Song, W.-L.; Wang, P.; Cao, L.; Anderson, A.; Meziani, M. J.; Farr, A. J.; Sun, Y.-P. *Angew. Chem. Int. Ed.* **2012,** 51, 6498-6501.

49.   Yao, Y.; Zeng, X.; Wang, F.; Sun, R.; Xu, J.-b.; Wong, C.-P. *Chem. Mater.* **2016,** 28, 1049-1057.

50.   Meziani, M. J.; Song, W.-L.; Wang, P.; Lu, F.; Hou, Z.; Anderson, A.; Maimaiti, H.; Sun, Y.-P. *ChemPhysChem* **2015,** 16, 1339-1346.

51.   Malekpour, H.; Chang, K. H.; Chen, J. C.; Lu, C. Y.; Nika, D. L.; Novoselov, K. S.; Balandin, A. A. *Nano Lett.* **2014,** 14, 5155-5161.

52.   Li, Q.; Guo, Y.; Li, W.; Qiu, S.; Zhu, C.; Wei, X.; Chen, M.; Liu, C.; Liao, S.; Gong, Y.; Mishra, A. K.; Liu, L. *Chem. Mater.* **2014,** 26, 4459-4465.

53.   Zeng, X.; Yao, Y.; Gong, Z.; Wang, F.; Sun, R.; Xu, J.; Wong, C. P. *Small* **2015,** 11, 6205-6213.

54.   Sato, K.; Horibe, H.; Shirai, T.; Hotta, Y.; Nakano, H.; Nagai, H.; Mitsuishi, K.; Watari, K. *J. Mater. Chem.* **2010,** 20, 2749-2752.

55.   Casalegno, V.; Vavassori, P.; Valle, M.; Ferraris, M.; Salvo, M.; Pintsuk, G. *J. Nucl. Mater.* **2010,** 407, 83-87.

56.   Xu, J.; Fisher, T. S. *Int. J. Heat Mass Transfer* **2006,** 49, 1658-1666.

57.   Jun, X.; Fisher, T. S. *IEEE Trans. Compon. Packag. Technol.* **2006,** 29, 261-267.

58.   Xu, J.; Fisher, T. S., Enhancement of thermal interface conductivities with carbon nanotube arrays. US Patent 8,093,715: 2012.

59.   Zhang, K.; Chai, Y.; Yuen, M. M. F.; Xiao, D.; Chan, P. *Nanotechnology* **2008,** 19, 215706.

60.   Culham, J.; Teertstra, P.; Savija, I.; Yovanovich, M. In *Design, assembly and commissioning of a test apparatus for characterizing thermal interface materials*, Thermal and Thermomechanical Phenomena in Electronic Systems, 2002. ITHERM 2002. The Eighth Intersociety Conference on, 2002; IEEE: pp 128-135.

61.   Leroy, B.; Plougonven, C. *J. Electrochem. Soc.* **1980,** 127, 961-970.

62. Draney, N. R.; Liu, J. J.; Jiang, T. In *Experimental investigation of bare silicon wafer warp*, Microelectronics and Electron Devices, 2004 IEEE Workshop on, 2004; IEEE: pp 120-123.

63. Due, J.; Robinson, A. J. *Appl. Therm. Eng.* **2013,** 50, 455-463.

64. Goel, N.; Anoop, T.; Bhattacharya, A.; Cervantes, J.; Mongia, R. K.; Machiroutu, S. V.; Lin, H.-L.; Huang, Y.-C.; Fan, K.-C.; Denq, B.-L. In *Technical review of characterization methods for thermal interface materials (TIM)*, Thermal and Thermomechanical Phenomena in Electronic Systems, 2008. ITHERM 2008. 11th Intersociety Conference on, 2008; IEEE: pp 248-258.

65. Vieira, C.; da Silva, P.; da Silva, F.; Capitaneo, J.; Monteiro, S. *Rev. Mater.* **2005,** 10, 526-536.

66. Mo, L.; Leong, K. K. M.; Kawi, S. *Catal. Sci. Tech.* **2014,** 4, 2107-2114.

67. Pang, L. S. K.; Saxby, J. D.; Chatfield, S. P. *J. Phys. Chem.* **1993,** 97, 6941-6942.

68. Xie, S.-Y.; Wang, W.; Fernando, K. A. S.; Wang, X.; Lin, Y.; Sun, Y.-P. *Chem. Commun.* **2005**, 3670-3672.

69. Tummala, R. R., *Fundamentals of microsystems packaging*. McGraw-Hill New York: 2001.

70. Tansley, T.; Maddison, D. *J. Appl. Phys.* **1991,** 69, 7711-7713.

71. Zhang, H. Y.; Zhang, X. W.; Lau, B.; Lim, S.; Ding, L.; Yu, M. *IEEE Trans. Compon. Packag. Manuf. Technol.* **2014,** 4, 807-816.

72. Lau, J. H., TSV Interposers: The Most Cost-Effective Integrator for 3D IC Integration. In *Chip Scale Rev*, 2011; Vol. 15, pp 23-27.

73. Hoe, Y. Y. G.; Yue, T. G.; Damaruganath, P.; Chong, C. T.; Lau, J. H.; Xiaowu, Z.; Vaidyanathan, K. In *Effect of TSV interposer on the thermal performance of FCBGA package*, Electronics Packaging Technology Conference, 2009. EPTC'09. 11th, 2009; IEEE: pp 778-786.

74. Sun, S.; Bao, J.; Mu, W.; Fu, Y.; Zhang, Y.; Ye, L.; Liu, J. In *Cooling hot spots by hexagonal boron nitride heat spreaders*, Electronic Components and Technology Conference (ECTC) , 2015 IEEE 65th, 26-29 May 2015, 2015; pp 1658-1663.

75. McLachlan, D. S. *J. Phys. C: Solid State Phys.* **1985,** 18, 1891.

76. Min, S.; Blumm, J.; Lindemann, A. *Thermochim. Acta* **2007,** 455, 46-49.

77. Heng Yun, Z.; Xiao Wu, Z.; Lau, B. L.; Lim, S.; Liang, D.; Yu, M. B. *IEEE Trans. Compon. Packag. Manuf. Technol.* **2014,** 4, 807-816.